AIAA JOURNAL
Vol. 43, No. 8, August 2005

Design of a Conformable Rotor Airfoil Using Distributed Piezoelectric Actuators

Phuriwat Anusonti-Inthra,* Roberto Sarjeant,† Mary Frecker,‡ and Farhan Gandhi§
Pennsylvania State University, University Park, Pennsylvania 16802

In the present study, several design methodologies are developed for determining the optimal distribution of a limited amount of piezoelectric material aft of the spar in a conformable rotor airfoil section. The design objectives are to maximize the trailing-edge deflection under actuation loads and simultaneously minimize the airfoil deflection under aerodynamic loads. Energy-like functions, mutual potential energy (MPE) and strain energy (SE), are used as measures of the deflections created by the actuation and aerodynamic loads, respectively. The design objectives are achieved by maximizing a multicriteria objective function that represents a ratio of the MPE to SE. Several design optimization techniques are evaluated including topology, geometry, sequential topology-geometry, and concurrent topology-geometry optimizations. The results of the study indicate that the optimized conformable airfoil section obtained using the concurrent topology-geometry optimization can produce a downward trailing-edge deflection equivalent to 4.24 deg of effective flap angle from the actuation loads, with the peak-to-peak deflection being nearly twice the downward deflection. The airfoil deformation caused by the aerodynamic loads alone is extremely small (less than 0.24 deg). Key features of the optimized airfoil are arrangement of actuators near the spar that act to stretch and shrink the skin and a bimorph like mechanism from midchord to the trailing edge. Additional results include a strain analysis, aerodynamic lift-and-drag increment study, and an examination of the effects of skin thickness and volume constraint of the active material.

Nomenclature

A_i	=	cross-sectional area of active element
$A_{\max}$	=	maximum limit of cross-sectional area
$A_{\min}$	=	minimum limit of cross-sectional area
C_p	=	pressure coefficient
c	=	airfoil chord
d_{33}	=	piezoelectric constant
E_i	=	modulus of elasticity
F_{act}	=	global load vector (actuation)
F_{aero}	=	global load vector (aerodynamic)
F_{dummy}	=	global load vector (dummy)
f^i_{act}	=	axial loading in a piezoelectric actuator
J	=	objective function
K	=	global stiffness matrix
l_i	=	length of an active element
p	=	aerodynamic pressure
t_c	=	thickness of piezoelectric layers
u	=	displacement field caused by actuation force
u_{tip}	=	downward tip deflection
V_i	=	applied voltage
V_∞	=	airfoil velocity
Vol	=	volume of active material
$\text{Vol}_{\max}$	=	maximum allowable volume of active material
v	=	displacement field caused by dummy load
w	=	displacement field caused by aerodynamic load
x_j	=	x coordinate of a node
y_j	=	y coordinate of a node
Δx_j	=	change in x coordinate
Δy_j	=	change in y coordinate
δ_{ref}	=	reference trailing deflection
ρ	=	air density

Received 28 March 2003; revision received 16 April 2004; accepted for publication 16 April 2004.

*Postdoctoral Fellow, Department of Aerospace Engineering. Member AIAA.
†Graduate Student, Department of Aerospace Engineering.
‡Associate Professor, Department of Mechanical and Nuclear Engineering.
§Associate Professor, Department of Aerospace Engineering. Member AIAA.

I. Introduction

THE blades of a helicopter main rotor are long and slender and flexible along the span but relatively rigid along the cross section. The airfoil cross section is rigid because any change in the airfoil shape caused by loading could significantly affect the aerodynamic performance. Although an uncommanded change in airfoil profile would obviously be undesirable, a deliberate change in airfoil shape induced intentionally could be exploited, for example, to ensure optimal performance, even as the flight condition varies. In addition to improving performance, a cyclic change in the airfoil profile over every rotor revolution could be used to generate unsteady aerodynamic loads that could cancel the vibratory loads on the rotor blades. In this respect, a continuously deformable, or conformable rotor blade airfoil would be a successor to rotor-blade airfoils with trailing-edge (TE) flaps, which are already being extensively considered for helicopter vibration reduction (for example, see Refs. 1–11). Virtually all of the research efforts focusing on rotor TE flaps for vibration reduction have used actuators constructed from piezoceramic material to deflect the flaps, because these actuators are solid state, compact, and can produce the required force at high frequency. However, the stroke of piezoelectric actuators is usually very small, so that a mechanical amplification of the stroke is necessary. Examples of these actuator-amplifier mechanisms include double-L piezostack actuators,[5] C-block actuators,[6,7] X-frame actuators,[8] and bimorph-lever benders.[10] Continuously conformable rotor airfoils will also be required to use a piezoelectric-based actuation system to meet the frequency requirements (other solid-state actuation concepts based on "smart" materials such as shape memory alloys do not have the required frequency bandwidth even though they can provide a larger stroke), whereas design optimization of the actuator and amplication mechanism could produce the required stroke amplification. Actuation mechanisms based on recently developed ferromagnetic shape memory alloys can also be of considerable interest in the future because the materials can produce large induced strain at high frequency.[12]

Continuously deformable airfoils have already been considered to improve performance and handling qualities (low-frequency

actuation) of fixed-wing aircrafts. For example, Saggere and Kota[13] suggested the use of passive compliant structures with a generic force actuator to produce static shape control of an airfoil camber, and Lagoudas and Strelec[14] considered the design of a reconfigurable wing actuated by shape memory alloy (SMA) wires in order to maximize lift-to-drag ratio. A flexible flap system using active deformable rib structures was studied as a part of DLR's Adaptive Wing Project and camber variations of ± 15 deg were achieved using an SMA tube.[15] Kudva et al.,[16] as a part of DARPA's Smart Wing program, developed deformable airfoil surfaces using ultrasonic piezoelectric motors and demonstrated that the airfoil could achieve trailing-edge deflections of up to 20 deg. Raney et al.[17] designed and tested a smooth adaptive wing with a variable thickness skin using SMA actuators. Achievable deflections were 8 and 3 deg for the trailing edge and leading edge, respectively. Despite the significant deflections, the SMA-based actuators would not be suitable for rotor vibration reduction because of their bandwidth limitation.

The philosophy for the design of a conformable airfoil can be adapted from the design of compliant mechanisms, which also achieve desired motion by undergoing elastic deformation.[18] One approach for designing compliant structures is to apply a topology design optimization method that determines the optimal distribution of available passive and/or active material within a design domain. Ananthasuresh et al.[19] has employed topology optimization for the design of compliant micro-electro-mechanical systems (MEMS). To maximize the geometric advantage or to maximize the mechanical efficiency, Frecker et al. developed a multicriterion topology optimization approach that had been applied for designing compliant hand-held devices[20] and compliant mechanical amplifiers for piezoelectric stack (d_{33}-type) actuators.[21] For multiple materials, a material interpolation scheme was developed for topology optimization of compliant mechanisms.[22] A two-stage optimization process was introduced by Kota et al.,[23] who proposed a second-stage size and shape optimization procedure that incorporated stress constraints on passive compliant elements. Additionally, several researchers have studied the topology optimization of different actuators, including a two-phase compliant actuator designed to maximize the work performed on an elastic workpiece[24] and flextensional actuators with piezoelectric material, where the topology of the passive material is optimized.[25]

II. Focus of the Present Study

The primary focus of the present study is to develop a design methodology for a smart material-based conformable rotor airfoil that could be used to provide cyclically controllable camber for helicopter vibration reduction. Methodologies using topology and geometry optimization for calculating the optimal distribution of active material within the airfoil section are developed and implemented. Key considerations are that the optimized airfoil section should produce significant trailing-edge deflection under actuation load while maintaining its shape under aerodynamic loading. The optimal designs are evaluated, and the mechanism by which the distributed active material produces the deformation is examined.

III. Analytical Model

In the present study the rotor blade is assumed to have a NACA-0012 airfoil section,[26] an aluminum skin of 1-mm thickness, and a chord length of 0.50 m. A rigid D-spar, the primary load-carrying member, extends from the leading edge of the airfoil to quarter-chord (Fig. 1a). The rigid D-spar is assumed not to undergo any deformation, and consequently, the section aft of the D-spar is clamped at quarter-chord, as presented in Fig. 1b.

To actuate the airfoil section at high frequency (in the range of 20 Hz for full-scale applications and higher frequencies for scaled model rotors), the active elements are chosen to be of piezoelectric ceramic material because of its fast response time. The stack actuator configuration, using the d_{33} effect, is chosen for its high force output. The active elements are distributed symmetrically about the centerline within the structure (as shown in Fig. 2), because both upward as well as downward deflections are necessary to generate the required unsteady aerodynamic loads to reduce vibration.

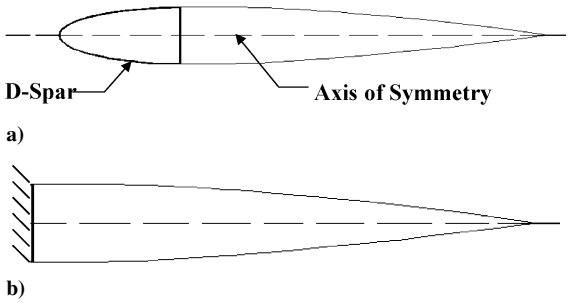

Fig. 1 Schematics of a) an NACA-0012 airfoil section and b) airfoil section with very rigid D-spar.

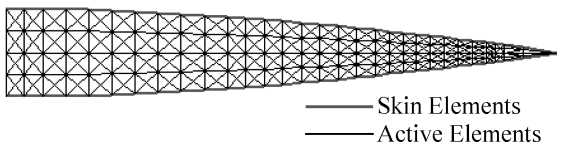

Fig. 2 Distribution of active elements within the ground structure.

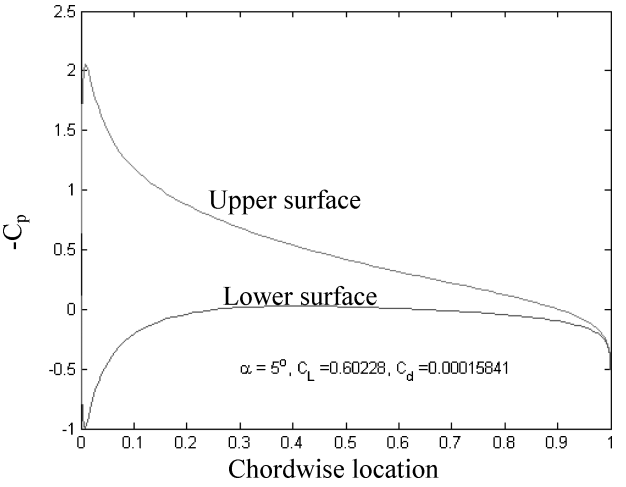

Fig. 3 Aerodynamic pressure distribution of the NACA-0012 at a 5-deg angle of attack.

The internal structure is modeled as a network of active elements called a ground structure. Each active element in the ground structure represents an individual stack actuator. Finite element modeling is employed to analyze the structure, with the skin modeled as frame elements that allow both bending and axial deformations, whereas the actuators are modeled as truss elements that have only axial deformation, with pinned connections between the successive frame-truss or truss-truss elements.

The equivalent axial loading generated by actuation of the ith active element can be expressed as follows:

$$f_{\text{act}}^{i} = E_i A_i d_{33} V_i / t_c \tag{1}$$

Equal and opposite voltages are applied to actuators located in the top and bottom sections of the structure to effectively generate bending loads on the structure. The displacement field induced by the active elements u is calculated using Eq. (2):

$$Ku = F_{\text{act}} \tag{2}$$

Aerodynamic loading of the airfoil section is calculated numerically using a linear-strength vortex panel method.[27] Figure 3 shows the variation of pressure coefficient C_p on the airfoil surfaces for the NACA 0012 airfoil at 5-deg angle of attack. The resulting aerodynamic pressure p at any point on the surface can then be calculated from this pressure coefficient using Eq. (3):

$$p = \tfrac{1}{2}\rho V_\infty^2 C_p \tag{3}$$

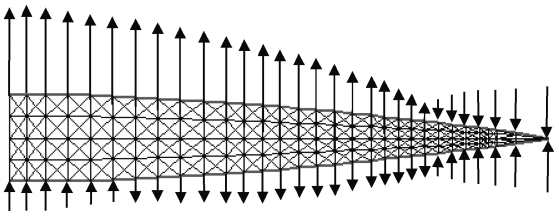

Fig. 4 Aerodynamic load distribution on the airfoil structure.

Using this surface pressure, the aerodynamic forces acting on a skin element can be determined by multiplying the surface pressure and the surface area of the skin element. Based on the aerodynamic forces, the aerodynamic loads acting at each node on the skin can be calculated. (The vertical nodal aerodynamic forces are shown graphically in Fig. 4.) The displacement field induced by these aerodynamic forces w is expressed in Eq. (4):

$$K w = F_{\text{aero}} \tag{4}$$

Although the aerodynamic loading would undergo variation as the airfoil deforms under the actuation loading, these variations are not considered in calculating F_{aero} in Eq. (4). This can be justified in the following terms: The reason for calculating the displacement in Eq. (4) is to ensure that when the material distribution within the airfoil section aft of the spar is varied during the design optimization process, the airfoil does not become overly flexible under aerodynamic loading. In this regard, the baseline aerodynamic surface-pressure distribution is adequate considering the perturbations in pressure distribution caused by variation in camber are not expected to a provide different conclusion. The differences in pressure distribution caused by the actuation voltage will be provided later in Sec. V.F for comparison. In addition, the results presented in Appendix A show that the differences in deflections obtained using the baseline and modified pressure distribution are small.

IV. Optimization Problem

A. Objective Function

The problem of achieving camber change is modeled as one of maximizing the vertical deflection at the trailing edge. The structure with maximum trailing-edge deflection, however, might be too flexible to withstand the aerodynamic loads, and so a multicriteria optimization problem is considered. The objective of the optimization problem is to simultaneously 1) maximize the vertical deflection at the trailing edge of the airfoil section caused by actuation load and 2) minimize the deflection of the entire airfoil section caused by aerodynamic load.

The first objective can be achieved by maximizing the mutual potential energy (MPE) of the structure.[28] Essentially, the MPE is a measure of ability of the actuation force to produce a specific deformation field. The MPE is defined as follows:

$$\text{MPE} = v^{\tau} K u = v^{\tau} F_{\text{act}} \tag{5}$$

where v is a reference displacement field created by a dummy load, which will be described by Eq. (7) defined later in this section, and u is the displacement field induced by the actuation force F_{act} [Eq. (2)]. Thus the first objective function can be written as

$$\max(J_1 = \text{MPE}) \tag{6}$$

To model the deflection at the trailing edge, the unit dummy load method is used. A unit load is applied in the downward vertical direction in order to deflect the trailing edge downward (Fig. 5), and a virtual displacement field v is calculated using Eq. (7):

$$K v = F_{\text{dummy}} \tag{7}$$

Although this first objective is to maximize downward deflection of the trailing edge when the actuators in the top section are positively charged and the actuators in the bottom section are negatively charged, because of the design's symmetry, an equivalent upward deflection of the trailing edge can be obtained by reversing the polarity of the actuation voltage. This will be demonstrated in Sec. V.E.

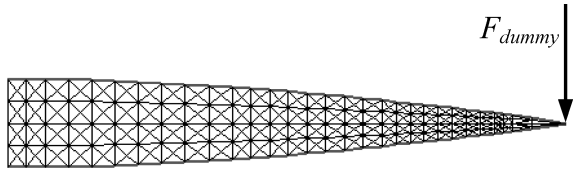

Fig. 5 Unit dummy load on the structure.

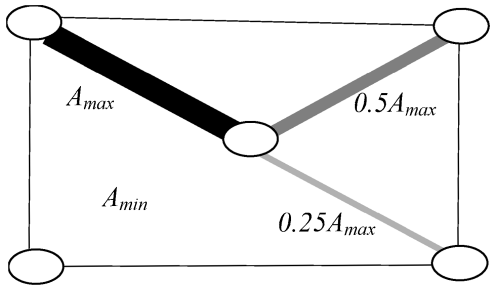

Fig. 6 Topology network of active elements, with different sizes.

For the second objective, strain energy (SE) is introduced as a measure of the deflection caused by the aerodynamic loads. The SE is defined as follows:

$$\text{SE} = \tfrac{1}{2} w^T K w \tag{8}$$

where w is described in Eq. (4). To facilitate the inclusion of this objective into one multicriteria objective function, it is desirable to modify this minimization of the SE into a maximization problem. The modified objective function can be expressed as

$$\max(J_2 = 1/\text{SE}) \tag{9}$$

The two objective functions are combined to form one multicriterion objective function using a ratio approach first proposed in Ref. 20 for passive compliant mechanisms. The objective function is defined as

$$\max(J = \text{MPE}/\text{SE}) \tag{10}$$

This type of objective function requires the use of a nonlinear optimization solution process.

B. Optimization Variables

Both the topology and the geometry of the ground structure shown in Fig. 2 are to be optimized. Topology optimization can be thought of as determining the optimal connectivity of active structural elements within the airfoil cross section. Geometry optimization consists of adjusting the location of the connection points between elements, while leaving the topology unchanged. In topology optimization, the cross-sectional areas of the active elements A_i are adjusted to maximize the objective function. This topology optimization will effectively increase the cross-sectional area of actuators that are highly effective and reduce the size of actuators that are less effective. Each variable A_i is bounded between a minimum and a maximum allowable value as follows:

$$0 < A_{\min} \leq A_i \leq A_{\max} \tag{11}$$

where $A_{\min}$ is nearly zero. An example of a topology network is shown in Fig. 6. The actuators that have reduced in size to reach the minimum limit are not shown in the figure but are included in the finite element analysis. The cross-sectional area of the skin elements is unchanged during this topology optimization. Another optimization constraint is the total amount of active material, which

is represented by active material volume defined as follows for M total active elements:

$$\text{Vol} = \sum_{i=1}^{M} l_i A_i \tag{12}$$

The volume constraint is expressed in terms of percentage of the maximum possible active material volume (e.g., $\text{Vol} = 0.50\,\text{Vol}_{\max}$), where

$$\text{Vol}_{\max} = \sum_{i=1}^{M} l_i A_{\max} \tag{13}$$

In geometry optimization, the nodal coordinates (x_i, y_j) of the active element network are modified to maximize the objective function. In essence, this geometry optimization will move nodes connecting the active elements to maximize their effectiveness (defined by the objective function). Modification of one nodal coordinate in an actuator network is shown schematically in Fig. 7. The change in nodal coordinates Δx_j and Δy_j is confined within coordinates of the neighboring nodes as described in Eq. (14):

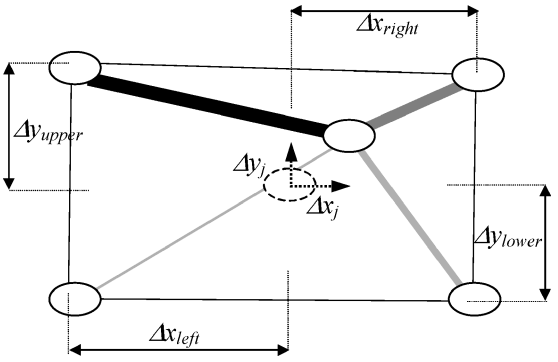

Fig. 7 Schematic of geometry modification of actuator network.

$$\Delta x_{\text{left}} \le \Delta x_j \le \Delta x_{\text{right}}$$
$$\Delta y_{\text{lower}} \le \Delta y_j \le \Delta y_{\text{upper}} \tag{14}$$

It is possible that the nodal coordinates of one node can coincide with those of another node. Nodal coordinates of the skin and the centerline elements are not modified in this geometry optimization.

In both topology and geometry optimization, the symmetry of the conformable airfoil structure about the axis of symmetry must be maintained because a similar amount of downward and upward deflections of the airfoil are required to produce the aerodynamic force for helicopter vibration reduction. This can be satisfied by imposing the symmetry condition as a constraint in the optimization process. This symmetry constraint could not be imposed in the structural analysis (using only half of the structure for analysis) because the aerodynamic loads are not symmetric.

C. Optimization Techniques

Several optimization techniques are considered in the present study. Topology optimization (Appendix B) followed by geometry optimization (Appendix C) is considered. Two more techniques combining the topology and geometry optimizations are examined: 1) sequential topology geometry and 2) concurrent topology-geometry optimizations. All of these techniques are explained in detail in this paper.

The flowchart of the topology optimization is presented in Fig. 8. This nonlinear optimization problem is solved using the sequential-linear-programming (SLP) algorithm, which is a gradient-based optimization method (requiring linearization of the objective function). Gradients of the objective function with respect to the topology variables are calculated analytically and are presented in Appendix B. The procedure starts with an initial topology, then the algorithm calculates the update in topology within a small move limit. The topology is updated iteratively until a convergence criterion is satisfied. Usually, the algorithm is converged when a change in objective function is less than 0.1% of its previous value.

The geometry optimization problem is also solved using the SLP algorithm, and the flowchart is given in Fig. 9. The procedure is

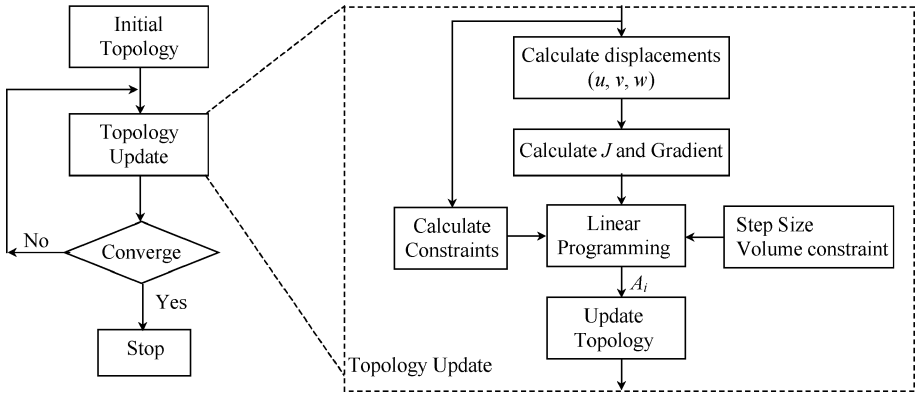

Fig. 8 Flowchart of the topology optimization process using the sequential-linear-programming algorithm.

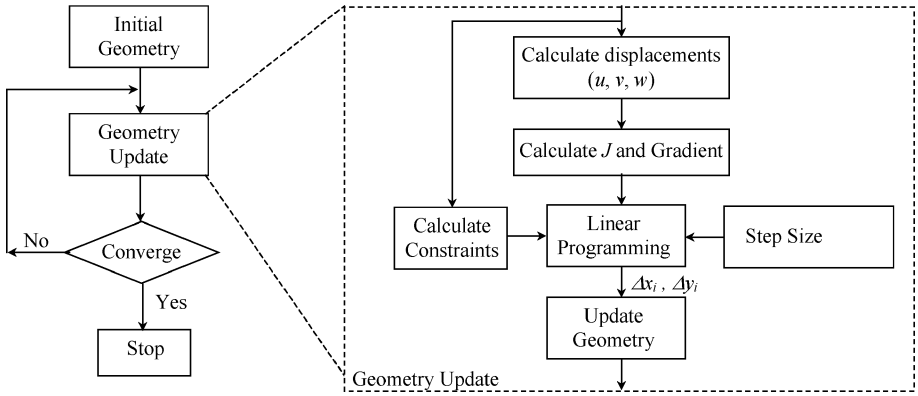

Fig. 9 Flowchart of the geometry optimization process using the SLP algorithm.

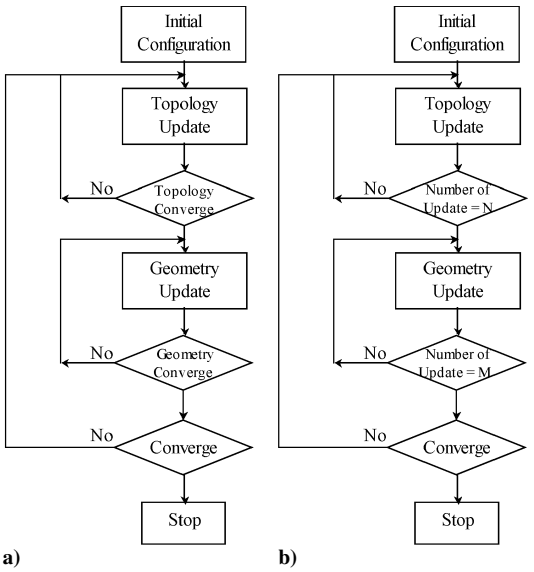

Fig. 10 Flowcharts of a) sequential and b) concurrent geometry-topology optimizations.

similar to that of the topology optimization. Again, the algorithm begins with an initial topology and geometry, and an appropriate change in the geometry is calculated using a small step size, while the topology remains fixed. The geometry update process repeats until the objective function is converged.

A sequential topology-geometry (STG) optimization is introduced to further improve the optimization process. Figure 10a shows the flowchart of this STG optimization. The algorithm starts with an initial configuration, and the topology optimization is performed on this initial configuration until it is topology optimized. Then the topology-optimized structure is used as an initial structure for the geometry optimization, which is carried out until converged. The geometry-optimized structure is sent back to the topology optimization, and the whole process repeats until a convergence criterion is met.

Another approach using concurrent topology-geometry (CTG) optimization is also introduced, and the flowchart of this CTG optimization is given in Fig. 10b. The algorithm is similar to that of the STG optimization, but instead of allowing the topology and geometry optimizations to converge to a suboptimal configuration the CTG optimization updates the topology and geometry of the structure a fixed number of iterations, N and M, respectively.

V. Results and Discussion

A. Ground Structure

The ground structure for the topology and geometry optimizations is shown in Fig. 2 and is made up of a network of truss and frame elements, with the properties presented in Table 1. The structure has 656 active truss elements representing piezoelectric ceramic stack actuators and 62 aluminum passive frame elements to model the skin. The topology optimization will determine the optimal cross-sectional area of the 656 active elements, but because of the symmetry of the problem there will be only 328 design variables for the topology optimization. After the optimization process it is expected that a number of active elements will have reached the lower limit, that is, the number of remaining active elements will be much less than the starting number of more than 600 elements.

B. Topology Optimization

Topology optimization is performed using the ground structure defined in Fig. 2. Five randomly generated sets of initial values of the design variables, the cross sections of the active elements, are used to avoid local minima. Each variable must be bounded within the allowable limit [see Eq. (11) and Table 2], and the total active material volume is constrained to 50% of $\text{Vol}_{\max}$ [defined in Eq. (13)]. The geometry of the structure is unchanged during the topology optimization.

Table 1 Properties of airfoil structure

Airfoil structure	Parameter	Value
Piezostack actuators (Truss elements)	Young's modulus E	60×10^9 N/m^2
	Applied voltage V_i	+150 V(upper) −150 V(lower)
	Piezoelectric constant d_{33}	640×10^{-12} m/V
	Thickness of piezoelectric layers t_c	0.00011 m
Airfoil section	Chord c	0.50 m
	Span	0.1 m
Airfoil skin (Frame elements)	Young's modulus E	30×10^9 N/m^2
	Cross-sectional area A	6.35×10^{-6} m^2
	Moment of inertia I	5.3×10^{-13} m^3
Aerodynamic properties	Air density ρ	1.225 kg/m^3
	Airfoil velocity V_∞	200 m/s

Table 2 Topology optimization constraints

Constraint	Value
$A_{\max}$	2.6×10^{-5} m^2
$A_{\min}$	1×10^{-9} m^2
Volume constraint	50% $\text{Vol}_{\max}$

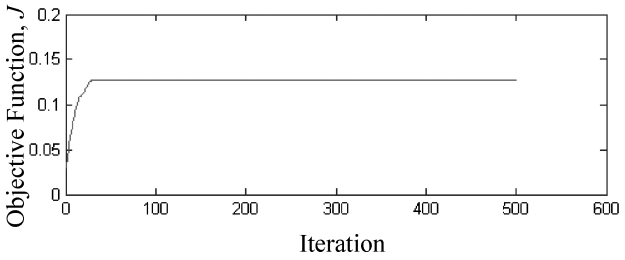

a) Convergence history

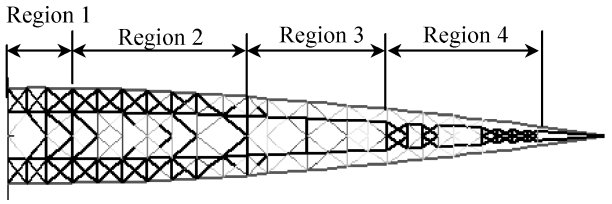

b) Optimized topology

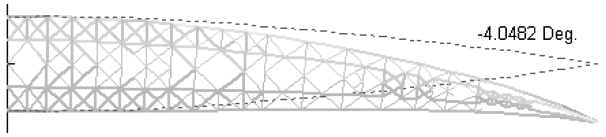

c) Deformation (7×) caused by actuation loads, with color-coded axial strain level

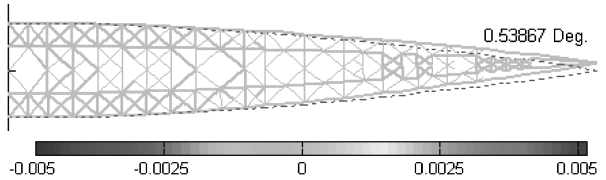

d) Deformation (7×) caused by aerodynamic loads, with color-coded axial strain level

Fig. 11 Topology optimization results with a volume constraint of 50% $\text{Vol}_{\max}$.

A set of results from the topology optimization is shown in Fig. 11. On average, it is observed that the optimization converges to an optimal topology, well within 100 iterations as shown by an example convergence history in Fig. 11a. The optimal topology is shown in Fig. 11b in grayscale. In this figure the active elements that have reduced in size to reach the minimum limit $A_{\min}$ are not shown, whereas those that have increased in size to reach the maximum limit $A_{\max}$ are shown as black thick lines, and the intermediate elements

are in shades of gray. For simplicity of interpretation, the airfoil section is divided into four regions: 1) an area close to quarter-chord, 2) an area near midchord, 3) an area from midchord to $\frac{3}{4}$-chord, and 4) an area from $\frac{3}{4}$-chord to the trailing edge (see Fig. 11b). The result shows that the active elements that are increased in size to reach $A_{\max}$ are concentrated in areas close to the skin in regions 1 and 2 and are less concentrated in region 3 and 4. The active elements that are reduced in size to reach $A_{\min}$ are in areas near the skin in regions 3 and 4, in area near the centerline in region 3, and are less concentrated throughout the areas near the symmetry axis in regions 1 and 2. As a physical observation, the active elements in regions 1 and 2 are arranged such that they produce a downward deflection of the trailing edge by stretching the upper skin and shrinking of the lower skin, and the arrangement of the active elements in regions 3 and 4 resembles a bimorph bender. Figures 11c and 11d, respectively, show the deformations caused by the actuation and aerodynamic loads of the optimized topology with corresponding axial strain level (color coded) in all of the elements. The displacement fields in Figs. 11c and 11d are exaggerated by a factor of 7 (7×) to improve the visualization of the deflections. With only the actuation loads, a downward tip deflection u_{tip} of 5.3 mm (8.33% of the thickness) was achieved. To compare this tip deflection with a flapped airfoil (with a hinge at 15% chord from the trailing edge), an equivalent flap angle (EFA) is introduced as follows:

$$\text{EFA} = a\tan(u_{\text{tip}}/0.15c) \tag{15}$$

The calculated EFA for this optimized topology is 4.05 deg. The strain level in the skin varies between 0.15–0.3% with the highest level occurring near the spar and the trailing edge. When subject to only the aerodynamic loads, very small deformation of the airfoil is observed, and the deflection is equivalent to 0.54-deg EFA.

The resulting optimized topologies obtained using randomly generated initial conditions (as well as a uniform distribution, all active elements are 50% of $A_{\max}$) are nearly identical. This demonstrates that the topology optimization likely converges to the global optima and that the solution is independent of the initial guess provided.

C. Geometry Optimization

Geometry optimization is performed using the geometry shown in Fig. 11b as an initial configuration, which can produce an EFA of 4.05 deg (and a J of 0.13). The cross-sectional areas of all elements are kept unchanged during the geometry optimization process. The results of the geometry optimization are shown in Fig. 12. The process converges after approximately 300 iterations as shown in Fig. 12a, with objective function increasing to 0.27 (a 100% increase from the original geometry), and the optimized geometry is shown in Fig. 12b. The geometry optimization produces an effective flap angle of 3.42 deg, which represents a 20% reduction from the original value.

The corresponding airfoil deflection caused by the aerodynamic loads alone is 0.24 deg. This suggests that the significant increase in objective function is caused primarily by reduction in the strain energy associated with the increase in stiffness of the structure. Using the four regions described earlier, the result shows little qualitative change in the distribution of the active material in regions 3 and 4. The active elements in regions 1 and 2 are shifted toward the skin emphasizing the mechanism that stretchs and shrinks the skins. The area between region 2 and 3 is a transition section connecting the bimorph-like mechanism (regions 3 and 4) to the active skin mechanism (region 1 and 2). The deformations and strain level caused by the actuation and aerodynamic loads are presented in Figs. 12c and 12d, respectively. In Fig. 12c, the skin strain level increases from 0.1% in regions 1 and 2 to 0.3% near the trailing edge.

D. STG Optimization

Results using the STG optimization are presented in this section. Essentially, the STG optimization is performing three complete series of topology-geometry optimizations (at which point convergence is achieved). To complete this, two more complete series of topology and geometry optimization are performed on the structure resulting from a complete topology-geometry optimization shown in Fig. 12b, which originally produced an objective function of 0.27,

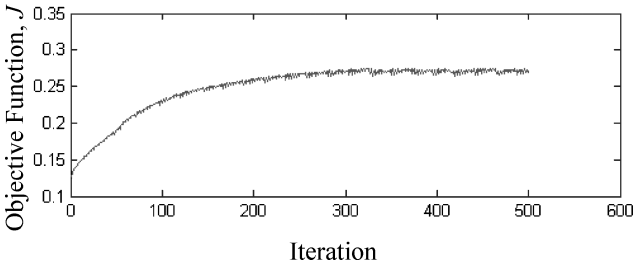

a) Convergence history

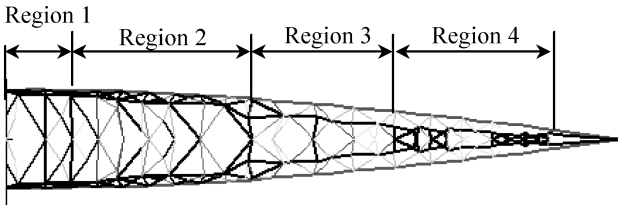

b) Optimized topology

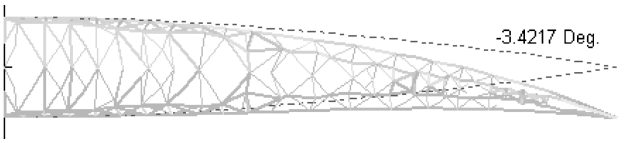

c) Deformation (7×) caused by actuation loads, with color-coded axial strain level

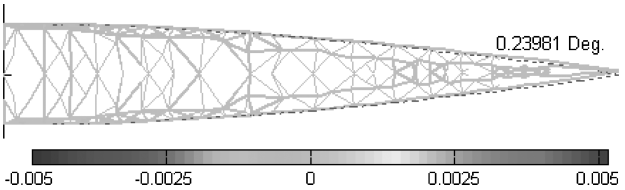

d) Deformation (7×) caused by aerodynamic loads, with color-coded axial strain level

Fig. 12 Geometry optimization results with a volume constraint of 50% $\text{Vol}_{\max}$.

and EFA of 3.42 deg. In the second and third topology-geometry optimization, the sizes and locations of all of the 656 active elements are still available to be optimized. The results of the STG optimization are presented in Fig. 13.

Figure 13a shows the convergence history of the additional series of topology-geometry optimizations, and it is observed that the STG optimization converges after three complete series of topology-geometry optimizations, with a maximum objective function of 0.35. The optimized structure (Fig. 13b) can produce the EFA of 3.83 deg (as opposed to 3.42 deg for the geometry optimized structure in Sec. V.C) under the actuation loads, and it is deflected 0.22-deg EFA under the aerodynamic loads. This again implies that the increase in the objective function is caused mostly by reduction in the strain energy. From Fig. 13b, the active elements that have reached $A_{\max}$ again are concentrated in areas close to the skin in regions 1 and 2 forming the active skin mechanism and in areas parallel to the skin in regions 3 and 4 forming a complex mechanism. The active elements that have reached $A_{\min}$ are scattered throughout the areas near centerline in regions 1–3. Similar to earlier observations, the arrangement of active elements in regions 1 and 2 is such that they produce a downward deflection of the trailing edge by stretching the upper skin and shrinking the lower skin. A slight difference in topology is observed when comparing the results from the geometry optimization (Fig. 12b) and STG optimization (Fig. 13b). The STG-optimized structure has more active elements in regions 3 and 4, especially near the skin, and the arrangements of the active mechanism near the centerline in region 1 are different.

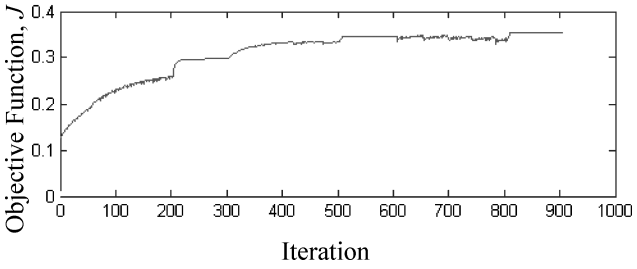

a) Convergence history

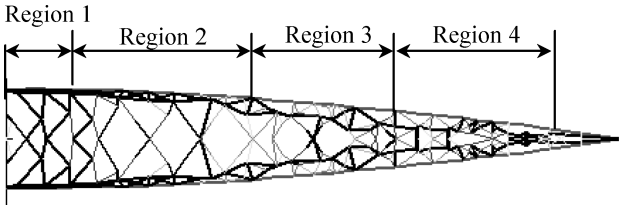

b) Optimized topology

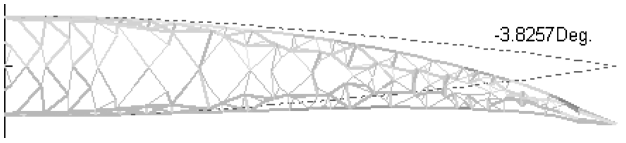

c) Deformation (7×) caused by actuation loads, with color-coded axial strain level

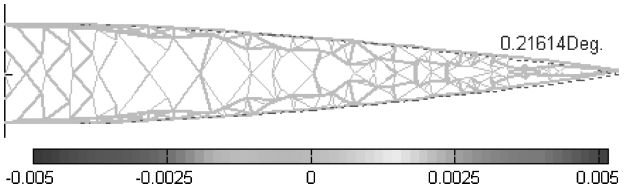

d) Deformation (7×) caused by aerodynamic loads, with color-coded axial strain level

Fig. 13 Sequential geometry-topology optimization results with a volume constraint of 50% Vol_{max}.

E. CTG Optimization

The concurrent optimization is performed using cycles of 21 iterations of topology optimization followed by 21 iterations of geometry optimization (i.e., N, M equal to 21). The initial configuration is the ground structure shown in Fig. 2 with a random distribution of active material. Results from the CTG optimization are presented in Fig. 14.

The convergence history (Fig. 14a) shows that the CTG optimization process converges after 1260 iterations (30 repetitions of the geometry and topology optimization cycles). The optimized structure, illustrated in Fig. 14b, can produce an EFA of 4.24 deg with an objective function of 0.35. The airfoil deformation caused by the aerodynamic loads is 0.24 deg. The CTG optimization results in a conformable airfoil that outperforms the airfoil obtained using the STG optimization in term of actuation angle. In comparison, the results obtained using STG and CTG optimizations are slightly different. The main distinction is that the CTG optimized structure has more active elements near the centerline in region 3. Deflection and axial strain level caused by only the actuation loads is shown in Fig. 14c. The skin strain level in region 1 is in the order of 0.1%, and the skin strain level increases along the chord with the maximum level of 0.4% near the trailing edge.

Because of the symmetry, for any of the optimized designs if the actuation voltages are reversed, that is, the actuators in the upper section receive negative voltage and the actuators in the lower section are positively charged, the conformable airfoil can produce an equal deflection in the opposite direction. This is seen in Fig. 15 for the CTG solution. An EFA of 4.24 deg is achieved in the upward direction, and this suggests that the conformable airfoil is capable of producing a peak-to-peak deflection of 8.48 deg.

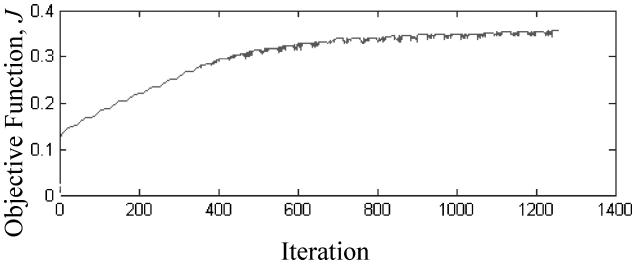

a) Convergence history

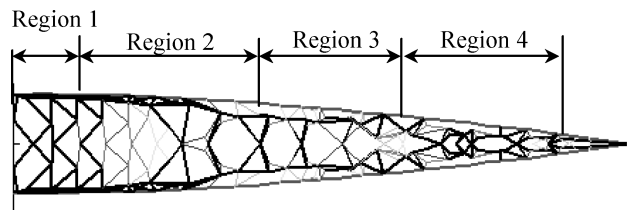

b) Optimized topology

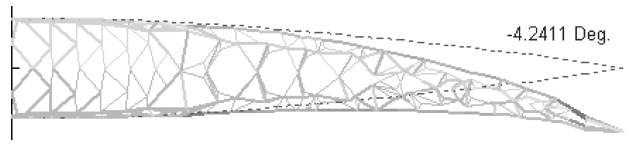

c) Deformation (7×) caused by actuation loads, with color-coded axial strain level

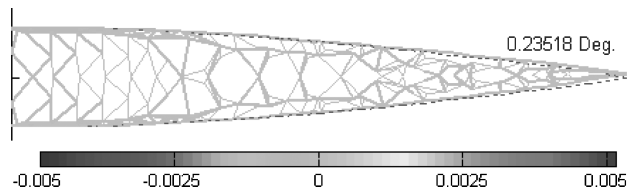

d) Deformation (7×) caused by aerodynamic loads, with color-coded axial strain level

Fig. 14 Concurrent geometry-topology optimization results with a volume constraint of 50% Vol_{max}.

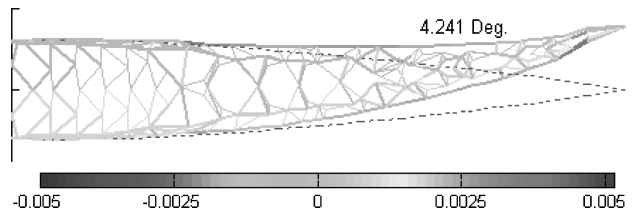

Fig. 15 Deformation (7×) caused by actuation loads with reverse polarity, color-coded axial strain level (CGT optimization with 50% Vol_{max}).

Even after concurrent topology and geometry optimization, the optimized structure is still complex and can be difficult to construct. The following sections present an effort to simplify the design by reducing the amount of active material and changing the thickness of the skin.

1. Effect of Active Material Volume Constraint

The effect of the volume constraint of the active material is examined in this section. All of the optimized structures are obtained using the CTG optimization at various volume constraint levels. Figure 16 shows optimized airfoil sections when the amounts of active material are 40, 30, 20, and 10% of Vol_{max}.

The complexity of the optimized structure is reduced as the volume constraint reduces. The active skin mechanism near the spar is only observed in the high (40 and 50%) volume constraint cases, whereas the bimorph-like mechanism is seen in all optimized structures with various volume constraint levels. The actuation and

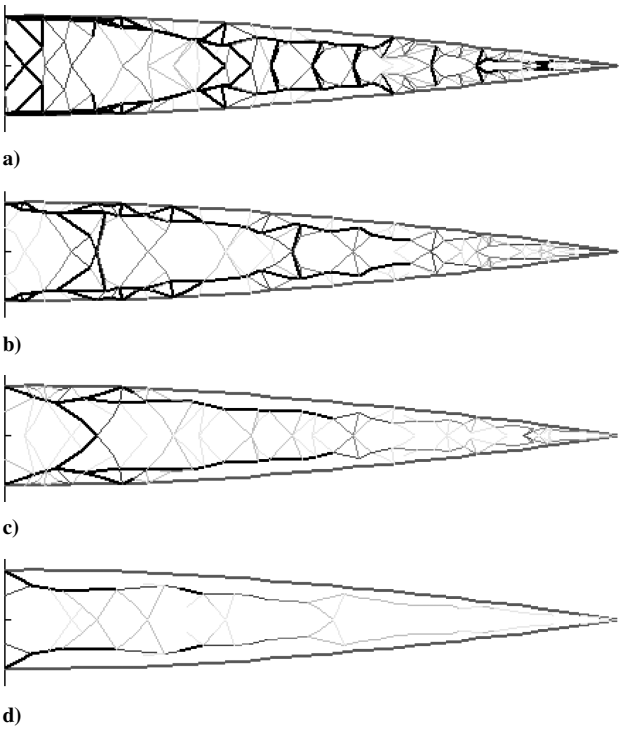

Fig. 16 Concurrent geometry-topology optimization results with volume constraints of a) 40, b) 30, c) 20, and d) 10% of Vol_{max}.

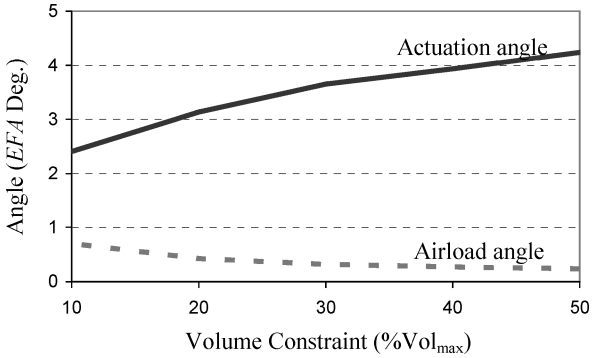

Fig. 17 Variations of actuation and airload angles obtained using CGT optimization.

airload angles (EFA) are presented in Fig. 17. As the volume constraint reduces from 50 to 10% of Vol_{max}, Fig. 17 shows that the actuation angle is decreased from 4.3 to 2.4 deg while the airload angle is increased from 0.2 to 0.8 deg. The structures with higher volume constraint have more active material and thus more weight. For example a conformable airfoil section with 20% of Vol_{max} weighs about 0.38 kg/cm, and a section with 50% volume constraint weighs 0.96 kg/cm.

2. Effect of Skin Thickness

The influence of skin thickness on the optimized topology is examined for the 20% volume constraint case. All of the optimized structures are obtained using the CTG optimization. Figures 18a–18d show the optimized structures when the skin thickness is 0.8, 0.6, 0.4, and 0.2 mm, respectively. In general, the optimized structures contain similar bimorph-like mechanisms running parallel to the skin. The actuation and airload angles for these structures are presented in Fig. 19. As the skin thickness decreases from 1 to 0.2 mm, the actuation angle is increased from 3.1 to 6.2 deg, and the airload angle is also increased from 0.42 to 0.88 deg. In the next section the conformable airfoil optimized with 20% volume constraint and skin thickness of 0.4 mm is chosen for further study on aerodynamic lift-and-drag increment.

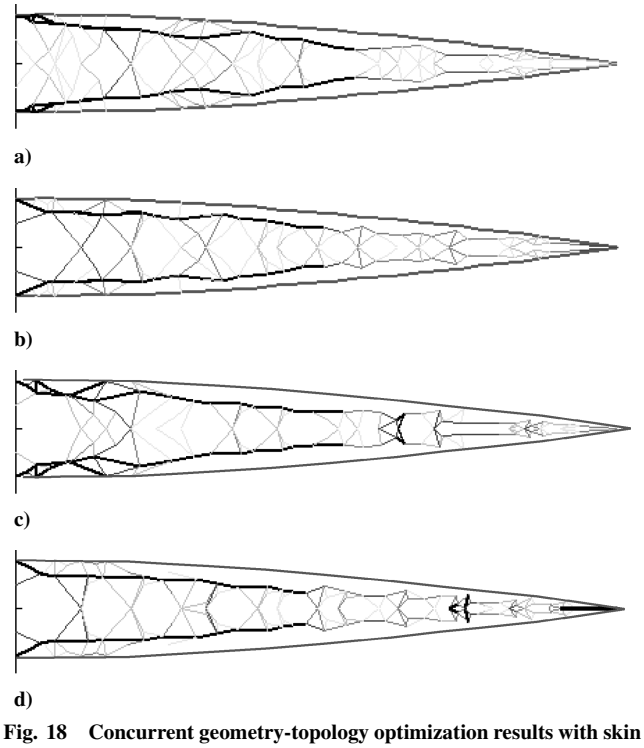

Fig. 18 Concurrent geometry-topology optimization results with skin thickness of a) 0.8, b) 0.6, c) 0.4, and d) 0.2 mm (20% Vol_{max}).

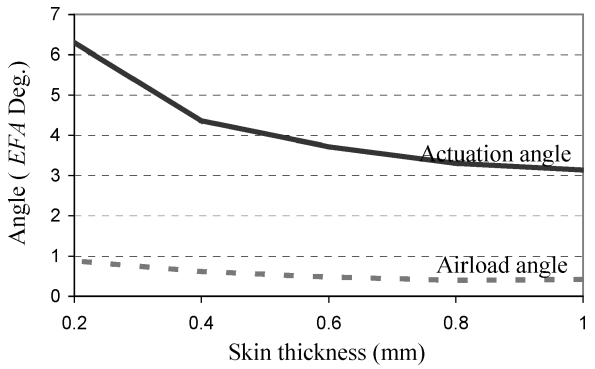

Fig. 19 Variations of actuation and airload angles obtained using CGT optimization as functions of skin thickness (20% Vol_{max}).

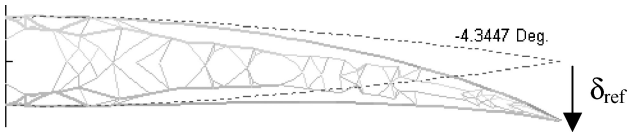

Fig. 20 Deformation (7×) caused by actuation loads, color-coded axial strain level (CGT optimization with 20% Vol_{max} and skin thickness of 0.4 mm).

F. Aerodynamic Lift-and-Drag Increment

This section investigates the aerodynamic lift-and-drag increment created by flapped and conformable airfoil sections from the baseline NACA 0012 airfoil section. The flapped airfoil section is fitted with a 15% chord trailing-edge flap, and the conformable airfoil section assumes a configuration shown in Fig. 20. (The airfoil section is obtained using CTG optimization with 20% volume constraint and skin thickness of 0.4 mm.)

The conformable airfoil can produce downward trailing-edge deflection of 5.7 mm (1.1% c) or 4.34-deg EFA. This trailing-edge deflection will be referred later as δ_{ref}. The increases in aerodynamic lift and drag are calculated using XFOIL ver. 6.94 (Ref. 29). In Ref. 29, the the pressure distribution is obtained by solving coupled inviscid/viscous flow equations over the airfoil simultaneously.

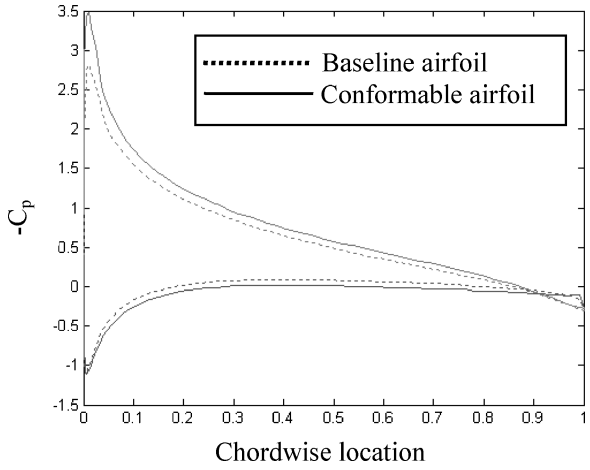

Fig. 21 Aerodynamic pressure distribution of airfoils at a 5-deg angle of attack for the baseline airfoil and conformable airfoil (when deflected at δ_{ref}) calculated by using XFOIL.

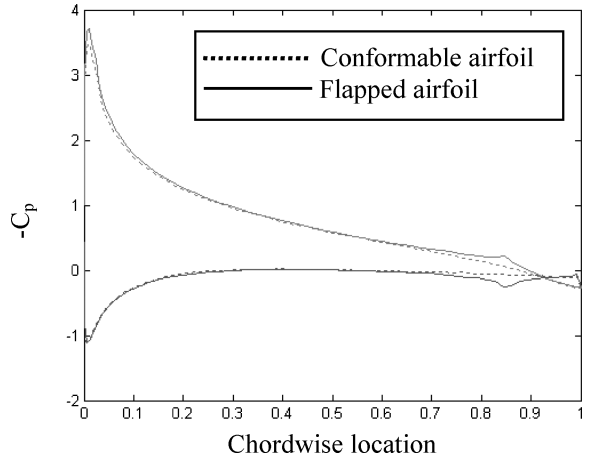

Fig. 22 Aerodynamic pressure distribution of the conformable and flapped airfoil at a 5-deg angle of attack (when deflected at δ_{ref}), calculated by using XFOIL.

The inviscid flow is modeled using linear-vorticity stream function panel method with a Karman–Stein compressibility correction, and the viscous flow in boundary layer and wake are accounted for using a surface transpiration model. The calculation is carried out at Reynolds number of 8.3864×10^6, Mach number of 0.6, and 5-deg angle of attack. Figure 21 shows the pressure distribution of the conformable and baseline airfoil sections. The lift-and-drag coefficients of the baseline airfoil are 0.6681 and 0.00703, respectively.

The profile of the pressure distributions is similar, but the magnitude of the pressures produced by the conformable airfoil is larger. The difference in the pressure distribution results in an increase in sectional lift of 25% from the baseline airfoil. The pressure distributions of both the flapped and conformable airfoils that have the same trailing deflection δ_{ref} are presented in Fig. 22. The pressure distributions from both airfoils are very similar except that the pressure for the flapped airfoil is slightly higher and there are variations in pressure near the flap hinge caused by the more sudden change in profile of the flapped airfoil.

Figure 23 shows the increment in sectional lift from the baseline airfoil for the flapped and conformable airfoils when they have the same trailing-edge deflection ranging from 0–100% of δ_{ref}. For both flapped and conformable airfoils the increments in sectional lift are increased linearly as the trailing-edge deflection increases, but the flapped airfoil always produces more lift than a conformable airfoil with the same trailing-edge deflection. For instance, when the trailing-edge deflection equals δ_{ref}, the flapped airfoil produce a lift increment of 35%, whereas the conformable airfoil can only increase the lift by 25% of the sectional lift of the baseline airfoil. The airfoil drag increment generated by the flapped and conformable airfoils is presented in Fig. 24. Aerodynamic drag caused by the flapped and conformable airfoils is increased almost linearly as the trailing-edge deflection increases. In general, the drag increment caused by the flapped airfoil is higher than that caused by the conformable airfoil for the same trailing-edge deflection. For example, when the trailing edge is δ_{ref} the drag increment caused by the flapped and conformable airfoils is 16 and 11% of the baseline airfoil, respectively.

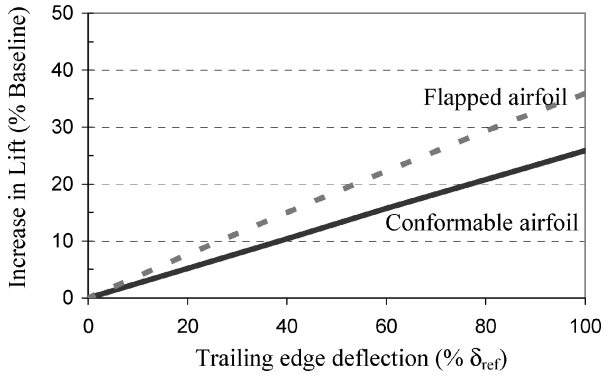

Fig. 23 Increment in lift caused by the flapped and conformable airfoils, calculated by using XFOIL.

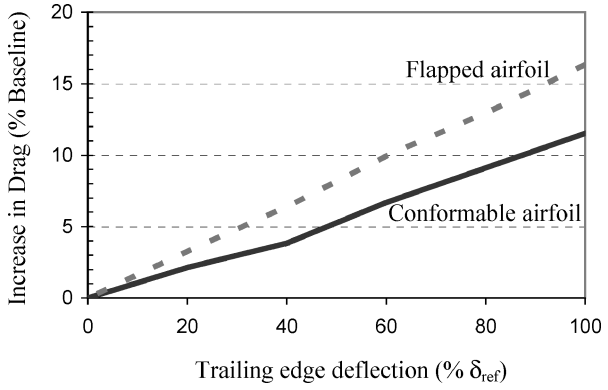

Fig. 24 Increment in drag caused by the flapped and conformable airfoils, calculated by using XFOIL.

G. Power Requirement

This section examines the power requirement of the conformable airfoil section assuming a configuration shown in Fig. 20 (CTG optimized with 20% volume constraint and skin thickness of 0.4 mm). The conformable airfoil produces downward trailing-edge deflection of 5.7 mm (9.2% of airfoil thickness) or 4.34-deg EFA under actuation loads and deflects upward 0.62-deg EFA under the airloads. The work done by the aerodynamic force is equal to the strain energy [Eq. (8)], and the work done by the actuation loads is equal to energy stored in the structure caused by the displacement generated by the actuation loads:

$$W_{act} = \tfrac{1}{2} u^T K u \tag{16}$$

The work done by the aerodynamic and actuation loads is calculated to be 0.02 and 0.5950 J, respectively. The estimated power requirement is simply the total work done as a result of the aerodynamic and actuation loads multiplied by the actuation frequency. Thus, for an actuation frequency of 20 Hz, the calculated power requirement is 12.3 W. However, the actual power required would be higher than this because of losses in the structure, actuators, and electrical circuits.

VI. Conclusions

Several optimization strategies for a conformable rotor airfoil using distributed piezoelectric actuators are developed and evaluated. The design optimization techniques determine optimal distribution of piezoelectric material aft of the rotor spar that simultaneously produce significant trailing-edge deflection under actuation loads, but minimal airfoil deflection under aerodynamic loads. This is achieved by optimizing a multicriteria objective function that contains a ratio of energy functions: mutual potential energy and strain energy, representing the deflections caused by the actuation and aerodynamic loads, respectively. Actuator topology and geometry are optimized using several techniques including topology, geometry, sequential topology geometry, and concurrent topology-geometry optimizations. Some of the key observations of the present study are summarized next.

Using the topology optimization, the optimized airfoil structure could produce a trailing-edge deflection equivalent to 4.05-deg effective flap angle (EFA) under actuation loads. The airfoil deflection caused by aerodynamic loads was small (0.54-deg EFA). Physically, the active elements near the spar were arranged such that they produced trailing-edge deflection by stretching and shrinking the skin, and the arrangement of the active elements from midchord to the trailing edge resembled a bimorph bender.

A slight improvement over the topology optimized structure was achieved using the geometry optimization, which produced an airfoil structure that underwent substantial smaller deformation (of 0.24 deg) under the aerodynamic loads, but also generated a slightly reduced EFA (of 3.42 deg) under the actuation loads. In the geometry optimization, the active elements near midchord were moved toward the skin, and the active elements between midchord and the trailing edge were almost unchanged. The sequential topology-geometry (STG) optimization produced an airfoil structure that was similar to the geometry optimized structure, except that more active material was added near the skin in the region between midchord and the trailing edge, and the arrangements of the actuators near the centerline close to the spar are different.

The optimized airfoil section using concurrent topology-geometry (CTG) optimization could produce an EFA of 4.24 deg under the actuation loads, and the deformation under the airload was 0.24 deg. Key features of this structure were similar to that of the STG optimized airfoil except that the CTG optimized structure had more active material near the centerline in midchord region.

The complexity of the actuator arrangement could be reduced by reducing the volume constraint of the active material, but the optimized conformable airfoil produced less actuation angle and deformed more under the aerodynamic loads. The reduction in actuation performance caused by less active material could be offset by decreasing the skin thickness, for example, the airfoil with 20% volume constraint and skin thickness of 0.4 mm could produce actuation angle of 4.34 or 8.86 deg peak to peak, but at the expense of deflection under airload (0.62 deg).

Appendix A: Effect of Aerodynamic Loads

This section investigates the effect of aerodynamic loading on the deflection generated by the actuation loads. The conformable airfoil section has a displacement field shown in Fig. 20. (The airfoil section is obtained using CTG optimization with 20% volume constraint and skin thickness of 0.4 mm.) The conformable airfoil can produce downward trailing edge deflection of 5.7 mm or 4.34-deg EFA without any aerodynamic loading. Using the vortex panel method,[27] pressure distributions of the baseline undeformed and the conformable airfoils are obtained and presented in Fig. A1. Then the total airfoil deflection is calculated using both the actuation and aerodynamic loads. The total deflections of the airfoil using the baseline pressure distribution are presented in Fig. A2a and Fig. A2b for the normal and reversed voltages, respectively. The total deflection using the baseline pressure distribution is equivalent to 3.68 deg, whereas the total deflection with pressure from the conformable airfoil is 3.12-deg EFA.

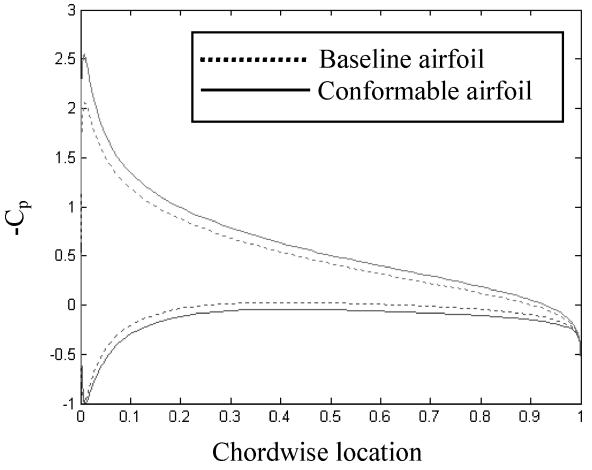

Fig. A1 Aerodynamic pressure distribution of airfoils at a 5-deg angle of attack for the baseline airfoil and conformable airfoil (when deflected at δ_{ref}), calculated using panel method.[27]

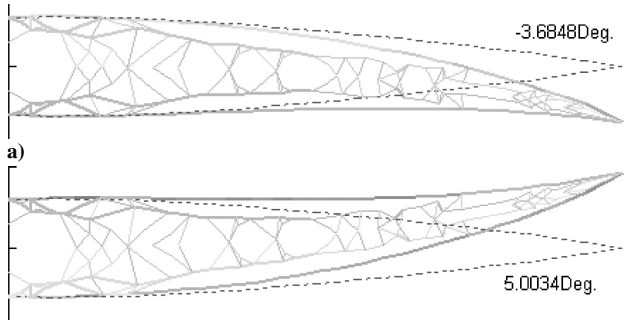

Fig. A2 Total airfoil deflection caused by both actuation and aerodynamic loads with baseline pressure distribution using a) normal voltage and b) reversed voltage.

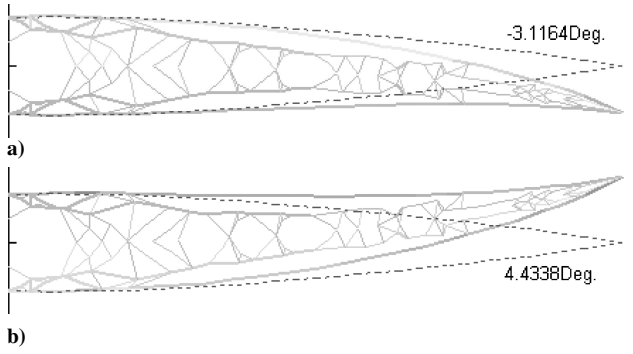

Fig. A3 Total airfoil deflection caused by both actuation and aerodynamic loads with pressure distribution from conformable airfoil using a) normal voltage and b) reversed voltage.

Appendix B: Sensitivity Analysis for Topology Optimization

The sensitivity or gradient of the objective function [Eq. (10)] with respect to airfoil topology variables A_i is provided in Eq. (B1):

$$\frac{\partial J}{\partial A_i} = \left(\mathrm{SE} \frac{\partial \mathrm{MPE}}{\partial A_i} - \mathrm{MPE} \frac{\partial \mathrm{SE}}{\partial A_i} \right) \Big/ \mathrm{SE}^2$$

$$\frac{\partial \mathrm{MPE}}{\partial A_i} = \frac{\partial v^T}{\partial A_i} K u + v^T \frac{\partial K}{\partial A_i} u + v^T K \frac{\partial u}{\partial A_i}$$

$$\frac{\partial \mathrm{SE}}{\partial A_i} = \frac{1}{2} \left(w^T \frac{\partial K}{\partial A_i} w + 2 w^T K \frac{\partial w}{\partial A_i} \right) \tag{B1}$$

Equation (B1) requires calculation of the derivative of the displacement fields and structural stiffness with respect to the topology variables, and they are given in Eq. (B2):

$$\frac{\partial u}{\partial A_i} = K^{-1}\left(\frac{\partial F_{\text{act}}}{\partial A_i} - \frac{\partial K}{\partial A_i}u\right)$$

$$\frac{\partial v}{\partial A_i} = K^{-1}\left(\frac{\partial F_{\text{dummy}}}{\partial A_i} - \frac{\partial K}{\partial A_i}v\right)$$

$$\frac{\partial w}{\partial A_i} = K^{-1}\left(\frac{\partial F_{\text{aero}}}{\partial A_i} - \frac{\partial K}{\partial A_i}w\right), \qquad \frac{\partial K}{\partial A_i} = \frac{k_i}{A_i} \quad \text{(B2)}$$

Here, k_i is the elemental stiffness matrix of the ith element. The derivatives of the active, aerodynamic, and dummy forces are provided in Eq. (B3):

$$\frac{\partial F_{\text{act}}}{\partial A_i} = \frac{f^i_{\text{act}}}{A_i}, \qquad \frac{\partial F_{\text{dummy}}}{\partial A_i} = 0, \qquad \frac{\partial F_{\text{aero}}}{\partial A_i} = 0 \quad \text{(B3)}$$

After substituting Eqs. (B3) and (B2) into Eq. (B1), the derivatives of the MPE and SE with respect to the topology variables are given by Eq. (B4):

$$\frac{\partial \text{MPE}}{\partial A_i} = v^T\frac{f^i_{\text{act}}}{A_i} - v^T\frac{k_i}{A_i}u, \qquad \frac{\partial \text{SE}}{\partial A_i} = -\frac{1}{2}w^T\frac{k_i}{A_i}w \quad \text{(B4)}$$

Appendix C: Sensitivity Analysis for Geometry Optimization

Similar to the approach discussed in Appendix B, the gradient of the objective function [Eq. (10)] with respect to geometry variables Δx_j and Δy_j can be calculated. This section provides only the derivation of the gradient with respect to Δx_j because an identical method can be applied to obtain the gradient with respect to Δy_j. The derivative of the objective function with respect to Δx_j is given by Eq. (C1):

$$\frac{\partial J}{\partial \Delta x_j} = \left(\text{SE}\frac{\partial \text{MPE}}{\partial \Delta x_j} - \text{MPE}\frac{\partial \text{SE}}{\partial \Delta x_j}\right)\Big/\text{SE}^2$$

$$\frac{\partial \text{MPE}}{\partial \Delta x_j} = \frac{\partial v^T}{\partial \Delta x_j}Ku + v^T\frac{\partial K}{\partial \Delta x_j}u + v^TK\frac{\partial u}{\partial \Delta x_j}$$

$$\frac{\partial \text{SE}}{\partial \Delta x_j} = \frac{1}{2}\left(w^T\frac{\partial K}{\partial \Delta x_j}w + 2w^TK\frac{\partial w}{\partial \Delta x_j}\right) \quad \text{(C1)}$$

Again, the derivatives of the displacement fields and structural stiffness (with respect to Δx_j) are required, and they can be calculated using Eq. (C2):

$$\frac{\partial u}{\partial \Delta x_j} = K^{-1}\left(\frac{\partial F_{\text{act}}}{\partial \Delta x_j} - \frac{\partial K}{\partial \Delta x_j}u\right)$$

$$\frac{\partial v}{\partial \Delta x_j} = K^{-1}\left(\frac{\partial F_{\text{dummy}}}{\partial \Delta x_j} - \frac{\partial K}{\partial \Delta x_j}v\right)$$

$$\frac{\partial w}{\partial \Delta x_j} = K^{-1}\left(\frac{\partial F_{\text{aero}}}{\partial \Delta x_j} - \frac{\partial K}{\partial \Delta x_j}w\right)$$

$$\frac{\partial K}{\partial \Delta x_j} = \sum_k \frac{\partial k_k}{\partial \Delta x_j} \quad \text{(C2)}$$

where k_k is the elemental stiffness matrix of the active elements that connect to the jth node. The derivatives of the active, aerodynamic, and dummy forces seen in Eq. (C2) are defined as follows:

$$\frac{\partial F_{\text{act}}}{\partial \Delta x_j} = \sum_k \frac{\partial f^k_{\text{act}}}{\partial \Delta x_j}, \qquad \frac{\partial F_{\text{dummy}}}{\partial \Delta x_j} = 0, \qquad \frac{\partial F_{\text{aero}}}{\partial \Delta x_j} = 0 \quad \text{(C3)}$$

where f^k_{act} is the elemental load vector of the active elements that attach to the jth node. By substituting Eqs. (C3) and (C2) into Eq. (C1), the derivatives of the MPE and SE with respect to Δx_j are summarized in Eq. (C4):

$$\frac{\partial \text{MPE}}{\partial \Delta x_j} = v^T\frac{\partial F_{\text{act}}}{\partial \Delta x_j} - v^T\frac{\partial K}{\partial \Delta x_j}u$$

$$\frac{\partial \text{SE}}{\partial \Delta x_j} = -\frac{1}{2}w^T\frac{\partial K}{\partial \Delta x_j}w \quad \text{(C4)}$$

Detail derivations of $\partial F_{\text{act}}/\partial \Delta x_j$ and $\partial K/\partial \Delta x_j$ are not provided here.

Acknowledgments

The authors gratefully acknowledge the support of the National Rotorcraft Technology Center through the Penn State Rotorcraft Center, with Yung Yu serving as the Technical Monitor.

References

[1]Milgram, J., Chopra, I., and Straub, F., "Rotors with Trailing Edge Flaps: Analysis and Comparison with Experimental Data," *Journal of the American Helicopter Society*, Vol. 43, No. 4, 1998, pp. 319–332.

[2]Bernhard, A. P. F., and Chopra, I., "Hover Testing of Active Rotor Blade-Tips Using a Piezo-Induced Bending-Torsion Coupled Beam," *Journal of Intelligent Material Systems and Structures*, Vol. 9, No. 12, 1998, pp. 963–974.

[3]Myrtle, T., and Friedmann, P., "Application of a New Compressible Time Domain Aerodynamic Model to Vibration Reduction in Helicopters Using an Actively Controlled Flap," *Journal of the American Helicopter Society*, Vol. 46, No. 1, 2001, pp. 32–43.

[4]Straub, F., and King, R., "Application of Smart Materials to Control of a Helicopter Rotor," *Proceedings of the Conference on Smart Structures and Materials*, Vol. 2721, edited by C. R. Crowe, Society of Photo-Optical Instrumentation Engineers, Bellingham, WA, 1996, pp. 66–77.

[5]Lee, T., and Chopra, I., "Design Issues of a High-Stroke, on-Blade Piezostack Actuator for a Helicopter Rotor with Trailing-Edge Flaps," *Journal of Intelligent Material Systems and Structures*, Vol. 11, No. 5, 2000, pp. 328–342.

[6]Clement, J. W., Brei, D., and Barret, R., "Wind Tunnel Testing of a High Authority Airspeed Insensitive Rotor Blade Flap," *Proceedings of the AIAA/ASME/ASCE/AHS/ASC Structures, Structural Dynamics, and Materials Conference and Exhibit*, Vol. 4, AIAA, Reston, VA, 1999, pp. 2414–2424.

[7]Chattopadhyay, A., Seeley, C. E., and Mitchell, L., "Design of a Smart Flap Using Polymeric C-Block Actuators and a Hybrid Optimization Technique," *Smart Materials and Structures*, Vol. 6, No. 2, 1997, pp. 134–144.

[8]Hall, S., and Tzianetopoulou, T., "Design and Testing of a Double X-Frame Piezoelectric Actuator," *Proceedings of the Conference on Smart Structures and Materials*, Vol. 3985, edited by N. W. Wereley, Society of Photo-Optical Instrumentation Engineers, Bellingham, WA, 2000, pp. 26–37.

[9]Straub, F., Ngo, H. T., Anand, V., and Domzalski, D., "Development of a Piezoelectric Actuator for Trailing Edge Flap Control of Full Scale Rotor Blades," *Smart Materials and Structures*, Vol. 10, No. 1, 2001, pp. 25–34.

[10]Koratkar, N. A., and Chopra, I., "Wind Tunnel Testing of a Smart Rotor Model With Trailing-Edge Flaps," *Journal of the American Helicopter Society*, Vol. 47, No. 4, 2002, pp. 263–272.

[11]Fulton, M., and Ormiston, R. A., "Hover Testing of a Small-Scale Rotor with On-Blade Elevons," *Journal of the American Helicopter Society*, Vol. 46, No. 2, 2001, pp. 96–106.

[12]Marioni, M. A., Bono, D. C., O'Handley, R. C., and Allen, S. M., "Pulsed Magnetic Field Actuation of Single-Crystalline Ferromagnetic Shape Memory Alloy Ni-Mn-Ga," *Proceedings of the Conference on Smart Structures and Materials*, Vol. 4699, edited by C. S. Lynch, Society of Photo-Optical Instrumentation Engineers, Bellingham, WA, 2002, pp. 191–194.

[13]Saggere, L., and Kota, S., "Static Shape Control of Smart Structures Using Compliant Mechanisms," *AIAA Journal*, Vol. 37, No. 5, 1999, pp. 572–578.

[14]Lagoudas, D., and Strelec, J., "Intelligent Design Optimization of a Shape Memory Alloy Actuated Reconfigurable Wing," *Proceedings of the Conference on Smart Structures and Materials*, Vol. 3984, edited by V. S. Varadam, Society of Photo-Optical Instrumentation Engineers, Bellingham, WA, 2000, pp. 338–348.

[15]Bein, Th., Hanselka, H., and Breitbach, E., "Adaptive Spoiler to Control the Transonic Shock," *Smart Materials and Structures*, Vol. 9, No. 2, 2000, pp. 141–148.

[16]Kudva, J., Sanders, B., Pinkerton-Florance, J., and Garcia, E., "Overview of DARPA/AFRL/NASA Smart Wing Phase 2 Program," *Proceedings of the Conference on Smart Structures and Materials*, Vol. 4332, edited by A. R. McGowan, Society of Photo-Optical Instrumentation Engineers, Bellingham, WA, 2001, pp. 383–389.

[17]Raney, D., Montgomery, R., Green, L., and Park, M., "Flight Control Using Distributed Shape-Change Effector Arrays," *Proceedings of the AIAA/ASME/ASCE/AHS/ASC Structures, Structural Dynamics, and Materials Conference and Exhibit*, Vol. 2, AIAA, Reston, VA, 2000, pp. 156–167.

[18]Ananthasuresh, G., and Kota, S., "Designing Compliant Mechanisms," *Mechanical Engineering*, Vol. 117, No. 11, 1995, pp. 93–96.

[19]Ananthasuresh, G. K., "Manufacturing Issues in Integrated Systems of Small Size," *Journal of Materials Processing and Manufacturing Science*, Vol. 8, April 2001, pp. 327–329.

[20]Frecker, M., Ananthasuresh, G. K., Nishiwaki, S., Kikuchi, N., and Kota, S., "Topological Synthesis of Compliant Mechanisms Using Multi-Criteria Optimization," *Journal of Mechanical Design*, Vol. 119, No. 2, 1997, pp. 238–245.

[21]Frecker, M., and Canfield, S., "Optimal Design and Experimental Validation of Compliant Mechanical Amplifiers for Piezoceramic Stack Actuators," *Journal of Intelligent Material Systems and Structures*, Vol. 2, No. 5, 2000, pp. 360–369.

[22]Yin, L., and Ananthasuresh, G., "Topology Optimization of Compliant Mechanisms with Multiple Materials Using a Peak Function Material Interpolation Scheme," *Structural and Multidisciplinary Optimization*, Vol. 23, No. 1, 2001, pp. 49–62.

[23]Kota, S., Hetrick, Z. Li, and Saggere, L., "Tailoring Unconventional Actuators Using Compliant Transmissions: Design Methods and Applications," *Transactions on Mechatronics*, Vol. 4, No. 4, 1999, pp. 396–408.

[24]Sigmund, O., "Design of Multiphysics Actuators Using Topology Optimization—Part II: Two-Material Structures," *Computer Methods in Applied Mechanics and Engineering*, Vol. 190, No. 5, 2001, pp. 6605–6627.

[25]Silva, E. C. N., Nishiwaki, S., and Kikuchi, N., "Topology Optimization design of Flextensional Actuators," *Transactions on Ultrasonics, Ferroelectrics, and Frequency Control*, Vol. 47, No. 3, 2000, pp. 657–671.

[26]Abbot, I. H., and Von Doenhoff, A. E., *Theory of Wing Sections*, Dover, New York, 1959, pp. 111–123.

[27]Katz, J., and Plotkin, A., *Low-Speed Aerodynamics: From Wing Theory to Panel Methods*, McGraw–Hill, New York, 1991, pp. 237–264.

[28]Shield, R. T., and Prager, W., "Optimal Structural Design for Given Deflection," *Journal of Applied Mathematics and Physics*, Vol. 21, No. 7, 1970, pp. 513–523.

[29]Drela, M., "XFOIL—An Analysis and Design System for Low Reynolds Number Airfoils," *Proceedings of the Low Reynolds Number Aerodynamics Conference*, edited by T. J. Mueller, Springer-Verlag, New York, 1989, pp. 1–12.

A. Messac
Associate Editor